Negative viscosity of liquid crystals in the presence of turbulence: Conductivity dependence, phase diagram, and self-oscillation

Fumiaki Kobayashi,[1] Yuji Sasaki,[1] Shuji Fujii,[1] Hiroshi Orihara,[1,*] and Tomoyuki Nagaya[2]
[1]*Division of Applied Physics, Hokkaido University, Sapporo 060-8628, Japan*
[2]*Division of Natural Sciences, Oita University, Oita 870-1192, Japan*

(Received 31 July 2019; accepted 15 January 2020; published 10 February 2020)

Recently, we reported the discovery of enormous negative viscosity of a nematic liquid crystal in the presence of turbulence induced by ac electric fields, which enabled us to observe unique phenomena related to the negative viscosity, such as spontaneous shear flow, hysteresis in flow curves, and self-oscillation [Orihara *et al.*, Phys. Rev. E **99**, 012701 (2019)]. In the present paper, we report the rheological properties of another nematic liquid crystal, which is a homologue of the previous one. The properties of the present liquid crystal are strongly dependent on electrical conductivity. Three samples with different conductivities were prepared by changing the amount of an ionic dopant. It was found that the lowest-conductivity sample without dopant shows no negative viscosity whereas the other ion-doped samples exhibit negative viscosity with strong dependence on the frequency of the ac electric field, consistent with microscopic observations. Phase diagrams of the negative- and positive-viscosity states in the amplitude and frequency plane are constructed to show the conductivity effect. Furthermore, we propose a model to reproduce another type of self-oscillation found in the present study.

DOI: 10.1103/PhysRevE.101.022702

I. INTRODUCTION

We recently discovered enormous negative viscosity of the nematic liquid crystal MBBA (*p*-methoxybenzylidene-*p*′-*n*-butylaniline) in the presence of turbulence induced by electric fields [1]. The viscosity of a fluid is a measure of its resistance to flow. Therefore, in the case of negative viscosity, the flow is amplified by negative resistance, even in the absence of external stress, resulting in spontaneous flow. Numerous experimental [2–9] and theoretical [10–20] studies have attempted to observe negative viscosity, mainly in magnetic fluids [7,8,16,17], electrorheological suspension [9,18–20], and active suspensions of bacteria [2–6,10–15,21–23]. Recently, active suspensions exhibit liquid crystalline order at high concentrations, have attracted much attention [13,15,21–23], and are theoretically predicted to show intriguing nonlinear rheological properties [13,15]. In suspensions of *Escherichia coli*, negative viscosity was first measured, although it was very low (approximately -10^{-1} mPa s) [5]. In contrast, MBBA exhibited much larger negative viscosity of -40 mPa s [1].

Taking advantage of the enormous negative viscosity of MBBA, we successfully observed several characteristic phenomena with a conventional rheometer [1]. We observed a spontaneous shear flow that rotated the upper disk of the rheometer, as well as reversal of the rotational direction upon application of an external torque in the opposite direction. The rotation speed ($\propto$ shear rate) was proportional to the square of the electric field amplitude. Hysteresis loops were also observed in the shear rate–shear stress curves under controlled shear stress, which were quite similar to those seen for ferroic materials such as ferromagnetics. As the frequency of the applied ac electric field was increased, the hysteresis loop or the negative viscosity vanished, indicating that a phase transition took place from a negative- to a positive-viscosity state. In this case, the frequency can be regarded as the temperature for ferroic materials. Thus, we coined the terms ferroviscosity, ferroviscous, and paraviscous. However, the ferroic materials are at equilibrium, whereas the liquid crystal is out of equilibrium and electric energy is constantly being supplied and partially converted into the spontaneous rotation. Under controlled shear rate, we observed S-shaped curves for the shear rate–shear stress measurements, where a negative slope, which confirms negative viscosity, was clearly seen at the origin. Theoretical consideration based on the Ericksen-Leslie theory revealed that the negative viscosity originates from the electric field–induced shear stress, which is generated by the rotation of the director in the presence of turbulence. In addition, we constructed a self-oscillator by attaching a coil spring to the upper disk of the rheometer, in which the spring exerts a restoring torque on the disk to convert the constant rotation to an oscillatory rotation. We would like to emphasize that MBBA is the only fluid known to possess such enormous negative viscosity.

In this paper, we report another nematic liquid crystal homologue of MBBA, EBBA (*p*-ethoxybenzylidene-*p*′-*n*-butylaniline), which exhibits properties similar to MBBA. However, the properties depend strongly on the conductivity of EBBA. For example, the negative viscosity vanishes in a low-conductivity sample. Therefore, we prepare three samples with different conductivities by changing the amount of an ionic dopant to examine the conductivity dependence. The conductivity affects the dependence on the frequency of the

*orihara@eng.hokudai.ac.jp

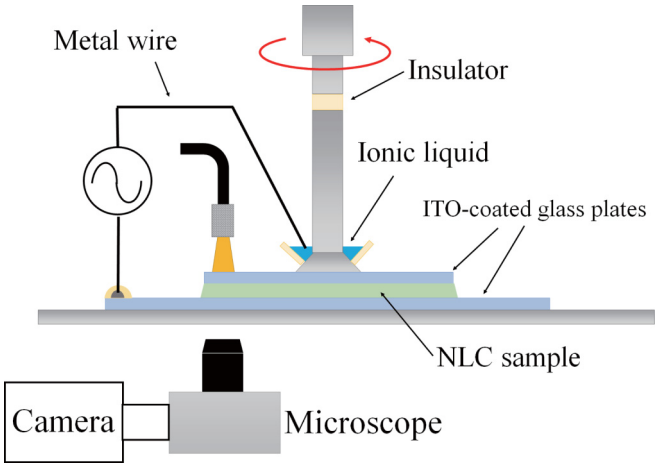

FIG. 1. Schematic of the experimental setup. The upper disk and bottom stage consist of glass coated with ITO. Microscopic observations are made through the bottom glass stage.

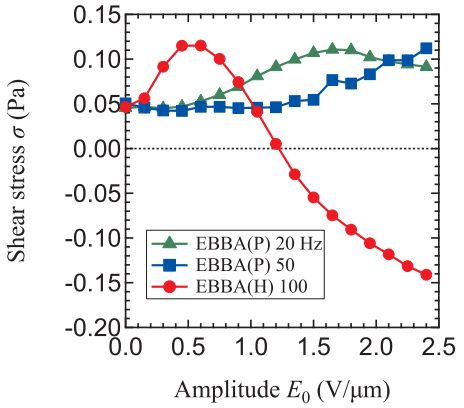

FIG. 2. Amplitude dependence of shear stress for EBBA(P) and EBBA(H), at a constant shear rate of $5\,s^{-1}$. The frequencies are 100 Hz for EBBA(H), and 20 and 50 Hz for EBBA(P). The shear stress is always positive at all electric fields for EBBA(P). However, the shear stress of EBBA(H) becomes negative at high electric fields ($E_0 > 1.2\,V/\mu m$).

ac electric field strongly; thus, we measure the rotation speed as a function of the amplitude and frequency of an ac electric field and construct a phase diagram consisting of the paraviscous (positive-viscosity) and ferroviscous (negative-viscosity) phases in the amplitude and frequency plane. Furthermore, we discuss another type of self-oscillation found in the EBBA system based on a model in which the viscoelasticity of EBBA is considered. This paper is organized as follows. In Sec. II, we describe the sample preparation and experimental setup. In Sec. III, we present the experimental results, including the electric field dependence of spontaneous shear stress, microscopic observations, S-shaped curves, phase diagrams, and self-oscillation. In Sec. IV, we discuss the mechanism of the self-oscillation mentioned in Sec. III by proposing a model including viscoelasticity. In Sec. V we summarize our findings.

II. EXPERIMENTAL DETAILS

The nematic liquid crystal (NLC) materials used were EBBA (Tokyo Chemical Industry) and MBBA (Tokyo Chemical Industry), both of which have negative dielectric anisotropy. EBBA exhibits the nematic-to-isotropic phase transition at 79.3 °C [24], and the dielectric anisotropy $\Delta\varepsilon$ is -0.26 at 50 °C [25]. We prepared the following three EBBA samples with different conductivities by doping with an ionic compound (tetrabutylammonium benzoate, Sigma-Aldrich): pure EBBA [EBBA(P)], low-doped EBBA [EBBA(L)], and high-doped EBBA [EBBA(H)]. The conductivities of these samples measured with unaligned cells at 1 kHz were 5.67×10^{-9}, 2.50×10^{-8}, and $1.28 \times 10^{-7}\,\Omega^{-1}\,m^{-1}$, respectively. The conductivity of EBBA(H) is comparable to that of pure MBBA [MBBA(P); $0.90 \times 10^{-7}\,\Omega^{-1}\,m^{-1}$], which was used as a reference.

A schematic of the experimental setup is shown in Fig. 1. The nematic liquid crystal samples were sandwiched between the bottom glass stage and the upper rotating glass disk attached to a rheometer (MCR302, Anton Paar). Since the shear rate depends on the measurement position for the parallel plates, we defined it as that at the edge of the upper disk, and the shear stress at the edge of the upper disk was calculated from the measured torque by assuming that the fluid is Newtonian. The surfaces of these glass plates were coated with indium tin oxide (ITO) to apply electric fields to the samples. No anchoring treatment was performed on the glass plates. The radius of the upper rotating glass disk, r, was 25 mm and the gap between the upper disk and the bottom stage, d, was 100 μm. An electric field was applied through a metal wire and ionic liquid [1-ethyl-3-methylimidazolium bis(trifluoromethanesulfonyl)imide] (Tokyo Chemical Industry) was placed in a vessel attached to the upper disk to prevent friction between the metal wire and upper disk. The temperature of the bottom glass stage was kept at 50.0 °C for EBBA and 25.0 °C for MBBA with a temperature controller (TDC-1600, Cell System). We applied an ac electric field, $E = E_0 \cos(2\pi f t)$, with an oscillator (WF1974, NF) and a high-voltage amplifier (T-HVA02, Turtle), the amplitude E_0 and frequency f of which were controlled with a PC to measure the E_0 and f dependences of shear rate $\dot{\gamma}$ and shear stress σ. Microscopic observations were made through the glass disk and stage using a microscope (IX73, Olympus) and a high-speed video camera (ORCA-Flash4.0, Hamamatsu). The samples were illuminated with a white LED (SLA-100A, Sigma Koki).

III. RESULTS

A. Negative shear stress

Figure 2 shows the electric field (amplitude E_0 of the applied ac electric field) dependence of shear stress under a constant shear rate of $5\,s^{-1}$ for EBBA(P) and EBBA(H) at 50 °C in the nematic phase, and at each electric field the shear stress was averaged for 200 s. The frequencies f were 100 Hz for EBBA(H), and 20 and 50 Hz for EBBA(P). The shear stress measured at 50 Hz in EBBA(P) monotonically increased with increasing applied electric field. At 20 Hz, the shear stress first increased to a maximum at $1.7\,V/\mu m$ and then decreased, but this decrease was small and the

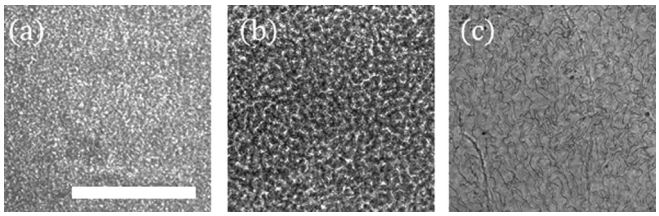

FIG. 3. Microscopic images observed (a) in EBBA(H) at $f = 100\,\mathrm{Hz}$ and $E_0 = 2.4\,\mathrm{V}/\mu\mathrm{m}$, and in EBBA(P) at (b) $f = 20\,\mathrm{Hz}$ and $E_0 = 2.4\,\mathrm{V}/\mu\mathrm{m}$ and (c) $f = 50\,\mathrm{Hz}$ and $E_0 = 2.4\,\mathrm{V}/\mu\mathrm{m}$. Although turbulence occurs in (a), (b), the pattern in (b) is coarser than that in (a). In (c) the sample contains many fluctuating disclinations without turbulence. The scale bar is 1 mm.

shear stress never became negative. No negative viscosity was observed in the frequency range of 0–2 kHz for EBBA(P). At 20 and 50 Hz the rheological properties of EBBA(P) were slightly different, but their structures were markedly different from each other and different from that of EBBA(H) at 100 Hz, as shown below. The shear stress for EBBA(H) first increased to a maximum at about $0.5\,\mathrm{V}/\mu\mathrm{m}$, and then decreased monotonically with increasing electric field, and the shear stress became zero around $1.2\,\mathrm{V}/\mu\mathrm{m}$ and negative as the electric field increased further. The behavior of EBBA(H) and EBBA(L) (results not shown) was similar to that of MBBA [1].

B. Microscopic observations under electric fields

The negative viscosity is closely related to electric field–induced turbulence [1]. Figure 3 shows the structures of EBBA(H) and EBBA(P) observed with a microscope. In EBBA(H), typical turbulence was observed at $f = 100\,\mathrm{Hz}$ and $E_0 = 2.4\,\mathrm{V}/\mu\mathrm{m}$ [Fig. 3(a)], where the viscosity was negative (Fig. 2). This image was taken in the steady state of dynamic scattering mode (DSM) 2, in which the fluid is in a turbulent state with disclinations [26–32]. In EBBA(P), turbulence was also observed at $f = 20\,\mathrm{Hz}$ and $E_0 = 2.4\,\mathrm{V}/\mu\mathrm{m}$ [Fig. 3(b)]. However, the pattern of EBBA(P) was coarser than that of EBBA(H), indicating that the turbulence in EBBA(P) was less developed compared with EBBA(H), which is thought to explain the absence of negative viscosity in EBBA(P). In contrast, at 50 Hz, EBBA(P) showed no turbulence [Fig. 3(c)], although it contained many fluctuating disclinations. These observations explain why the shear stress of EBBA(P) monotonically increased at 50 Hz but began to decrease at 20 Hz (Fig. 2). At 20 Hz, the electrically induced turbulence reduced the shear stress at high electric field strength, which was so weak that the shear stress remained positive.

C. N-shaped curve and scaling relation

We examined whether the scaling relation between the shear stress σ and the shear rate $\dot{\gamma}$ observed in MBBA(P) also holds in EBBA(H). Figure 4(a) shows the $\dot{\gamma}-\sigma$ curves measured at a frequency of 100 Hz and various electric field strengths (amplitudes) at controlled shear rate, where the sampling time was 10 s at each shear rate. In Fig. 4(a), the average value of shear stress is plotted as a function of shear rate. N-shaped curves were clearly observed at large electric fields (0.9–$2.4\,\mathrm{V}/\mu\mathrm{m}$). In our previous paper [1], we referred to the curves as the S-shaped curves instead of N-shaped curves because the $\dot{\gamma}$ and σ axes were reversed. The N-shaped curves were observed in the ferroviscous phase, whereas monotonically increasing curves (0–$0.6\,\mathrm{V}/\mu\mathrm{m}$) were observed in the paraviscous phase [1]. The N-shaped curves reveal the occurrence of negative viscosity because the slope around the origin is negative ($d\sigma/d\dot{\gamma} < 0$). The fact that the slope at the origin is almost independent of the electric field in the ferroviscous phase implies the validity of the scaling relation, as explained in our previous paper [1].

The scaling relation between σ and $\dot{\gamma}$ was derived from dimensional analysis in the ferroviscous phase [1] as

$$\frac{\gamma_1 \dot{\gamma}}{\varepsilon_0 |\Delta\varepsilon| E_0^2} = f\left(\frac{\sigma}{\varepsilon_0 |\Delta\varepsilon| E_0^2}\right), \tag{1}$$

where γ_1 is the rotational viscosity and $f(x)$ is a scaling function. The scaled data from Fig. 4(a) are plotted in Fig. 4(b),

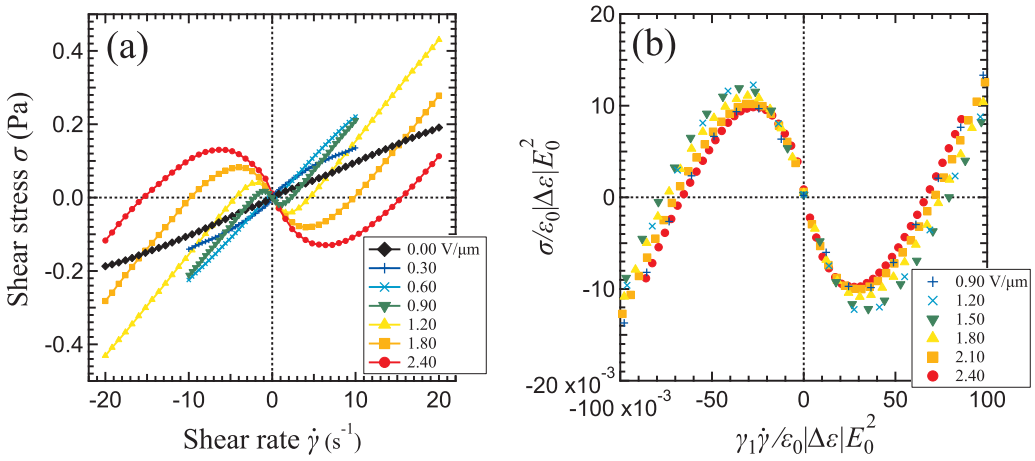

FIG. 4. N-shaped curves and scaling relation in EBBA(H). (a) $\dot{\gamma} - \sigma$ curves under a controlled shear rate for various amplitudes of ac electric field at $f = 100\,\mathrm{Hz}$. (b) Relationships between scaled shear rate and scaled shear stress based on the data shown in (a). The scaling relation holds at large electric fields ($E_0 > 0.90\,\mathrm{V}/\mu\mathrm{m}$) in the ferroviscous phase. Here, $\gamma_1 = 0.057$ (Pa s) and $\Delta\varepsilon = -0.26$ [24,25].

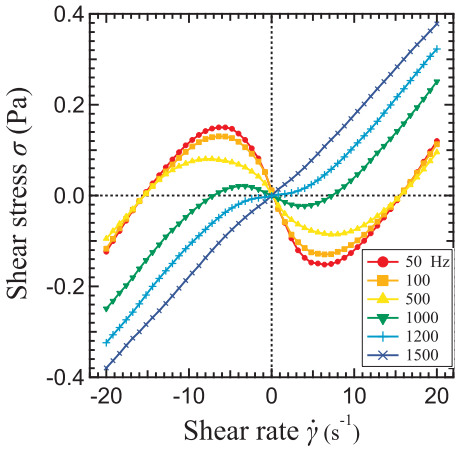

FIG. 5. Frequency dependence of N-shaped curve at $E_0 = 2.40\,\mathrm{V}/\mu\mathrm{m}$ in EBBA(H). The slope (viscosity) at the origin in the ferroviscous phase is negative and it gradually decreases with increasing frequency.

which shows that scaling relation (1) holds at large electric fields in the ferroviscous phase. This scaling relation also held for EBBA(L) and MBBA(P).

Figure 5 shows the frequency dependence of the $\dot{\gamma}-\sigma$ curve of EBBA(H) at $E_0 = 2.40\,\mathrm{V}/\mu\mathrm{m}$ as the frequency was increased. The transition from the ferroviscous to paraviscous phase was observed. The slope at the origin, which gives the viscosity, gradually decreased with increasing frequency. Similar frequency dependence was also observed for EBBA(L) and MBBA(P).

D. Spontaneous shear rate and phase diagram

The negative shear viscosity in the ferroviscous state can generate spontaneous shear flow, resulting in the rotation of the upper disk of the rheometer if the disk can rotate freely, that is, under zero shear stress. Figure 6 shows the spontaneous shear rate $\dot{\gamma}_s$ as a function of E_0^2 at $f = 50$ Hz

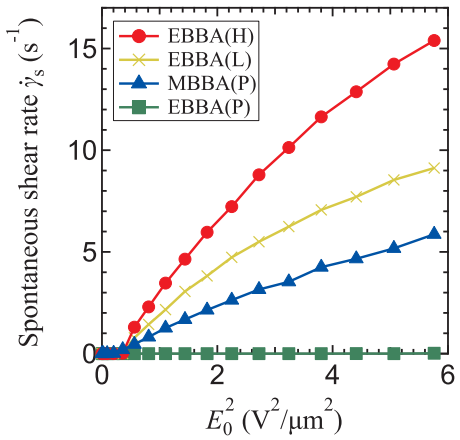

FIG. 6. Dependences of spontaneous shear rate (proportional to the angular velocity of the upper rotating disk) on the square of the amplitude, E_0^2, at $f = 50$ Hz for EBBA(P), EBBA(L), EBBA(H), and MBBA(P). The measurements are performed at zero shear stress. The samples other than EBBA(P) show spontaneous shear flow.

under zero shear stress, where the shear rate was measured for a period of 200 s at each electric field, and the average value was plotted. In EBBA(P), no spontaneous shear flow was observed because it has no negative viscosity in the measured range of electric field. The other samples showed a similar dependence of spontaneous shear rate on electric field. There was a critical electric field, which corresponds to the paraviscous to ferroviscous phase transition point, over which the spontaneous shear rate monotonically increased. However, it should be noted that shear rate periodically oscillated in EBBA(H), which was behavior markedly different from that of EBBA(L) and MBBA(P) around the transition point. The oscillation period was much smaller than the measurement time, so the oscillation was averaged out, and $\dot{\gamma}_s = 0$ in Fig. 6. The oscillation is discussed in detail in Sec. IV. For steady rotation, EBBA(H) had the largest spontaneous shear rate, which was about three times larger than that of MBBA(P). In our previous paper, the spontaneous shear rate was proportional to the square of the electric field amplitude in the high electric field region and the proportionality arose from the scaling relation described by Eq. (1); substitution of $\sigma = 0$ into Eq. (1) yields $\dot{\gamma} \propto E_0^2$. In Fig. 6, MBBA(P) shows good proportionality, whereas EBBA(L) and EBBA(H) do not.

Figure 7(a) shows the frequency dependence of spontaneous shear rate $\dot{\gamma}_s$ for EBBA(L), EBBA(H), and MBBA(P) at $E_0 = 2.10\,\mathrm{V}/\mu\mathrm{m}$. For all samples, the spontaneous shear rate reached a maximum, and then dropped to zero at critical frequency f_c. The fluid was in the ferroviscous state below f_c and in the paraviscous state over f_c. The f_c values at $E_0 = 2.10\,\mathrm{V}/\mu\mathrm{m}$ were 160, 1100, and 470 Hz for EBBA(L), EBBA(H), and EBBA(P), respectively. In addition to the voltage dependence, near the critical frequency the shear rate of EBBA(H) oscillated. The amplitude and frequency dependence of the spontaneous shear rate were examined with a two-dimensional plot of $\dot{\gamma}_s$ in the $E_0 - f$ plane for each sample [Figs. 7(b)–7(d)], giving the phase diagram consisting of the paraviscous and ferroviscous phases, where we included the oscillation state in the paraviscous phase. The measurements were taken at 17 amplitudes and 20 frequencies [indicated by white and red dots in Fig. 7(c)], and the interpolated data were plotted. The phase diagrams show that the ferroviscous phase appeared at high amplitudes and low frequencies in the three samples, although the lowest amplitude and the highest frequency depended on the sample. The amplitudes and frequencies were $0.68\,\mathrm{V}/\mu\mathrm{m}$ and 160 Hz for EBBA(L), $0.60\,\mathrm{V}/\mu\mathrm{m}$ and 1100 Hz for EBBA(H), and $0.53\,\mathrm{V}/\mu\mathrm{m}$ and 470 Hz for MBBA(P). For EBBA, the lowest amplitude of EBBA(H) was almost the same as that of EBBA(L), whereas the highest frequency of EBBA(H) was much higher than that of EBBA(L). The large difference in f_c can be explained if f_c is only related to the electrical relaxation time given by the ratio of the dielectric constant and the conductivity. For this assumption, f_c may be inversely proportional to the electrical relaxation time, that is, $f_c \propto \bar{\sigma}/\bar{\varepsilon}$, where we neglect the anisotropies in dielectric constant and conductivity, and the bars indicate averages. Because $\bar{\varepsilon}$ is the same for the two samples, f_c may be just proportional to $\bar{\sigma}$. The ratio of f_c of EBBA(H) to EBBA(L) is 6.5, whereas that of $\bar{\sigma}$ is 5.1, indicating that the difference in f_c mainly comes from the difference in the electrical relaxation time. A

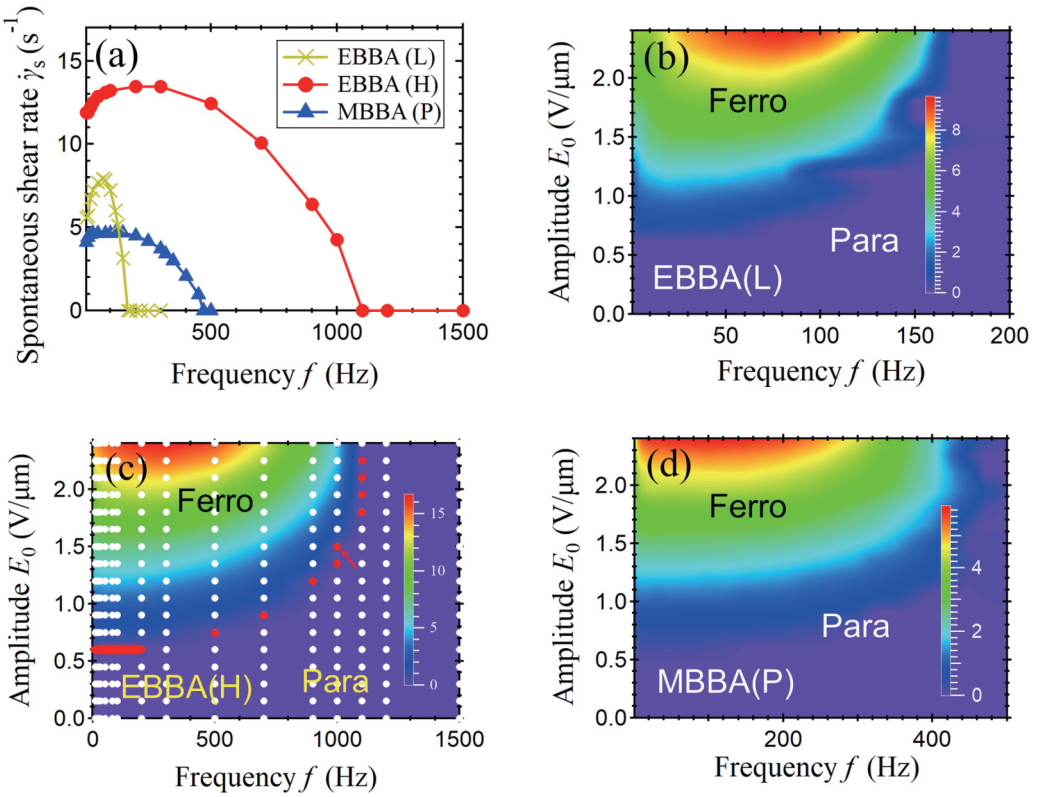

FIG. 7. (a) Frequency dependences of spontaneous shear rate $\dot{\gamma}_s$ at $E_0 = 2.10\,\mathrm{V}/\mu\mathrm{m}$ for EBBA(L), EBBA(H), and MBBA(P). (b)–(d) Phase diagrams for the paraviscous and ferroviscous phases in the $E_0 - f$ plane for EBBA(L), EBBA(H), and MBBA(P). The measurement points are indicated by white and red dots only in (c); the oscillation is observed at the red dots. The ferroviscous phase appears at high amplitudes and low frequencies for all three samples. The zigzag boundaries are due to the lack of data points.

similar conductivity dependence was theoretically shown for electrohydrodynamic convection [33,34].

The shear rate oscillation was observed in the narrow region near the boundary between the paraviscous and ferroviscous phases [red dots in Fig. 7(c)] in EBBA(H), although it was not observed in the other samples. Figure 8 shows the temporal changes in shear rate at three frequencies at 1.50 V/μm. At 1000 Hz [red arrow in Fig. 7(c)], self-oscillation was observed, where amplitude A and period T were 0.34 s^{-1} and 16 s, respectively. In contrast, at 900 Hz, the self-oscillation changed to spontaneous steady rotation, whereas at 1100 Hz neither behavior was observed.

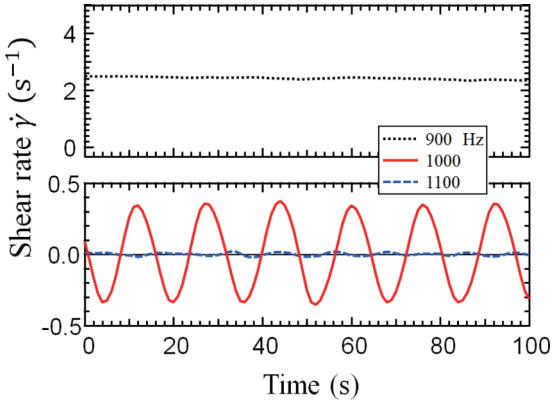

FIG. 8. Temporal changes in shear rate for three typical frequencies at $E_0 = 1.50\,\mathrm{V}/\mu\mathrm{m}$. At $f = 900\,\mathrm{Hz}$, the shear rate is constant and its value is 2.5 s^{-1}. At $f = 1000\,\mathrm{Hz}$, the shear rate temporally oscillates and amplitude A is about 0.34 s^{-1} and period T is about 16 s. At $f = 1100\,\mathrm{Hz}$ in the paraviscous phase, the oscillation disappears.

IV. DISCUSSION

A. Model for self-oscillation

In this section, we discuss the mechanism of the self-oscillation shown in Sec. III. In our previous study [1], similar oscillation occurred when we attached a coil spring to the shaft of the upper disk. In that case, the oscillation is caused by the restoring force of the spring. In the present case, however, there is no spring. An important difference is that in the spring system, the oscillation occurs around a position at which the restoring force vanishes, whereas in the system without the spring, the oscillation occurs around any position because there is no special position. Furthermore, the oscillation in the present system changes to steady rotation when the electric field is increased or the frequency is decreased. Thus, we need a model with a restoring force but no special center for oscillation. We construct such a model by combining a nonlinear rheological element with negative viscosity (N-shaped element) and the Maxwell element, which consists of a spring (an elastic element) with shear modulus G_M, connected in series to a viscous dashpot (viscous element)

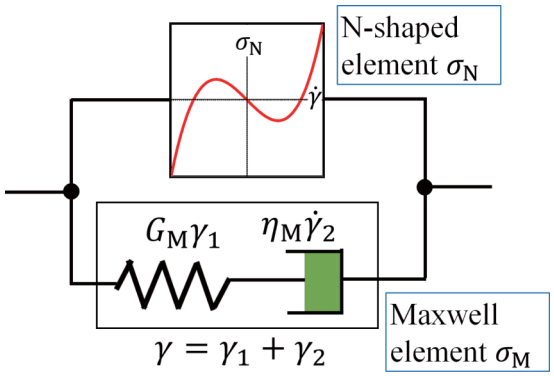

FIG. 9. Model consisting of a nonlinear rheological element (N-shaped element) and the Maxwell element with a viscous dashpot and an elastic spring.

with shear viscosity η_M (Fig. 9). We discuss the origin of the elasticity included in the Maxwell element in Sec. IV C.

In the model, the equation of motion for the upper disk is expressed in terms of strain γ as

$$I\ddot{\gamma} = -\sigma_N - \sigma_M + \sigma, \tag{2}$$

$$\dot{\sigma}_M = -\frac{1}{\tau}\sigma_M + G_M\dot{\gamma}, \tag{3}$$

where σ_N and σ_M are the shear stresses of the nonlinear element with negative viscosity and the Maxwell element, respectively, and the rotation angle of the upper disk ϕ is given by $\phi = a_\phi\gamma$ ($a_\phi = h/r$, where h is the gap and r is the radius of the upper disk), and torque M exerted on the upper disk from the liquid crystal is given by $M = a_M(\sigma_N + \sigma_M)$ ($a_M = \pi r^3/2$). I corresponds to the inertia I_P of the upper disk and is given by $I = (a_M/a_\phi)I_P$, and σ corresponds to the torque exerted on the upper disk by the rheometer. $\tau = \eta_M/G_M$ is the relaxation time of the Maxwell element.

B. N-shaped curve and phase diagram

We consider the $\dot{\gamma}-\sigma$ curve shown in Sec. III obtained under controlled shear rate. For this case, Eqs. (2) and (3) become

$$\sigma = \sigma_N + \sigma_M, \tag{4}$$

$$\sigma_M = \tau G_M\dot{\gamma} = \eta_M\dot{\gamma}. \tag{5}$$

Therefore, the shear stress measured under controlled shear rate is given by

$$\sigma = \sigma_N + \eta_M\dot{\gamma}. \tag{6}$$

This means that the measured stress is increased by the viscous part, $\eta_M\dot{\gamma}$, of the Maxwell element. In contrast, when $\dot{\gamma}$ changes quickly or the relaxation time is large, we can neglect the first term of the right-hand side of Eq. (3), so that $\dot{\sigma}_M = G_M\dot{\gamma}$, that is, $\sigma_M = G_M\gamma$ because a constant of integration can be omitted without loss of generality for the present system. By substituting $\sigma_M = G_M\gamma$ into Eq. (2) with $\sigma = 0$, we get

$$I\ddot{\gamma} = -\sigma_N - G_M\gamma, \tag{7}$$

resulting in our previous model with a coil spring, which produces the oscillation. We approximate σ_N as a cubic function of $\dot{\gamma}$ for simplicity,

$$\sigma_N = a\dot{\gamma} + b\dot{\gamma}^3, \tag{8}$$

where $b > 0$. Substitution of Eq. (8) into Eq. (7) yields

$$\sigma = (a + \eta_M)\dot{\gamma} + b\dot{\gamma}^3. \tag{9}$$

This equation indicates that the N-shaped curve appears when $a + \eta_M < 0$, and therefore it cannot always appear, even when the viscosity of σ_N is negative ($a < 0$).

Now, we consider the self-oscillation under controlled shear stress of $\sigma = 0$. For convenience, we scale Eqs. (2) and (3) with Eq. (8) and $\sigma = 0$,

$$\frac{d^2\tilde{\gamma}}{d\tilde{t}^2} = -\tilde{a}\frac{d\tilde{\gamma}}{d\tilde{t}} - \left(\frac{d\tilde{\gamma}}{d\tilde{t}}\right)^3 - \tilde{\sigma}_M, \tag{10}$$

$$\frac{d\tilde{\sigma}_M}{d\tilde{t}} = -\tilde{\sigma}_M + \tilde{G}_M\frac{d\tilde{\gamma}}{d\tilde{t}}, \tag{11}$$

introducing the scaled quantities

$$\tilde{t} = \frac{t}{\tau}, \quad \tilde{\gamma} = \sqrt{\frac{b}{I\tau}}\gamma, \quad \tilde{\sigma}_M = \sqrt{\frac{b\tau^3}{I^3}}\sigma_M,$$

$$\tilde{a} = a\frac{\tau}{I}, \quad \tilde{G}_M = G_M\frac{\tau^2}{I}. \tag{12}$$

We construct a phase diagram consisting of the static state ($d\tilde{\gamma}/d\tilde{t} = 0$), the oscillation state, and the steady rotation state ($d\tilde{\gamma}/d\tilde{t} =$ constant) in the $\tilde{a} - \tilde{G}_M$ plane based on Eqs. (10) and (11). First, we examine the linear stability of the static state. Setting $\tilde{\gamma} = \tilde{\gamma}_0\exp[\tilde{\lambda}\tilde{t}]$, and $\tilde{\sigma}_M = \tilde{\sigma}_{M_0}\exp[\tilde{\lambda}\tilde{t}]$ and omitting the cubic term in Eq. (10), $\tilde{\lambda}$ is obtained as

$$\tilde{\lambda} = \frac{-(\tilde{a}+1) \pm \sqrt{(\tilde{a}+1)^2 - 4(\tilde{a} + \tilde{G}_M)}}{2}. \tag{13}$$

In Fig. 10, the stable region of the static state ($\mathrm{Re}[\tilde{\lambda}] < 0$) is shown in blue. As $\tilde{a}$ decreases, the system undergoes a transition from the static state to the oscillation state ($\mathrm{Im}[\tilde{\lambda}] \neq 0$, red region) for $\tilde{G}_M > 1$, or to the steady rotation state ($\mathrm{Im}[\tilde{\lambda}] = 0$, yellow region) for $\tilde{G}_M < 1$. In the oscillation state, numerical calculations showed that the steady rotation state appears as $\tilde{a}$ decreases further (Fig. 10). The broken black line in Fig. 10 was obtained by linear stability analysis of the steady rotation state. Because the transition between the oscillation and steady rotation states is of first order (discontinuous), the stability limit line goes over the coexisting line obtained by the numerical calculations. The change in E_0 and f in the experiment may correspond mainly to that of $\tilde{a}$ in Fig. 10. As $\tilde{a}$ decreases, for $\tilde{G}_M < 1$, only a direct transition to the steady rotation state occurs (blue solid line in Fig. 10), whereas for $\tilde{G}_M > 1$, the transition occurs through the oscillation state (red solid line). Thus, the transition for $\tilde{G}_M < 1$ corresponds to EBBA(L) and MBBA(P), and the transition for $\tilde{G}_M > 1$ corresponds to EBBA(H).

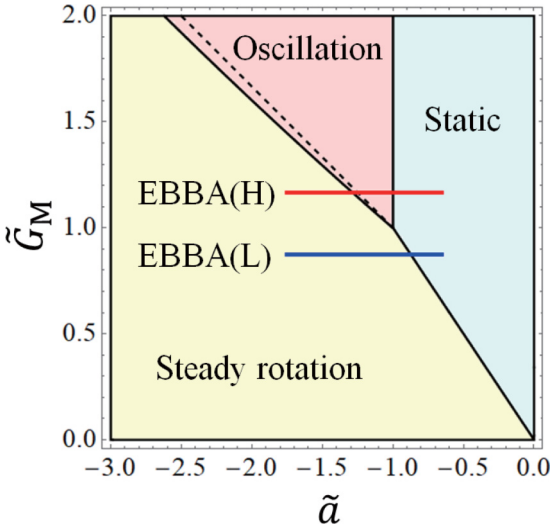

FIG. 10. Phase diagram consisting of the static state (blue), oscillation state (red), and steady rotation state (yellow) in the $\tilde{a} - \tilde{G}_M$ plane. The broken black line was obtained by linear stability analysis of the steady rotation state.

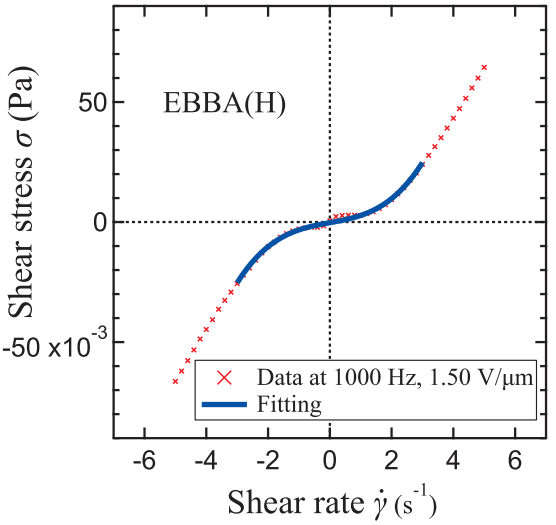

FIG. 11. $\dot{\gamma}-\sigma$ curve measured at $f = 1000\,\mathrm{Hz}$ and $E_0 = 1.50\,\mathrm{V}/\mu\mathrm{m}$. The solid blue line indicates the fitting result from Eq. (9) with $a + \tau G_M = 3.2 \times 10^{-3}$ Pa and $b = 5.1 \times 10^{-4}\,\mathrm{Pa\,s^2}$.

C. Analysis of experimental results

To analyze the experimental data, we find an approximate solution for the oscillation state from Eqs. (10) and (11) by assuming

$$\tilde{\gamma}(\tilde{t}) = \tilde{A}\cos(\tilde{\omega}_0\tilde{t}), \tag{14}$$

where $\tilde{A}$ and $\tilde{\omega}_0$ are the amplitude and the angular frequency of oscillation, respectively. When the transition to the oscillation state occurs ($\tilde{G}_M > 1$), the transition point is given by $\tilde{a} = -1$, and thus, $\tilde{\omega}_0$ at the transition point is obtained from Eq. (13) as

$$\tilde{\omega}_0 = \frac{\sqrt{(\tilde{a}+1)^2 - 4(\tilde{a}+\tilde{G}_M)}}{2i} = \sqrt{\tilde{G}_M - 1}. \tag{15}$$

Hereafter, for simplicity we assume that $\tilde{\omega}_0$ is given by Eq. (15) independent of $\tilde{a}$. For Eq. (14), the stationary solution of Eq. (11) becomes

$$\tilde{\sigma}_M(\tilde{t}) = \tilde{A}\tilde{G}_M \frac{\tilde{\omega}_0[\tilde{\omega}_0\cos(\tilde{\omega}_0\tilde{t}) - \sin(\tilde{\omega}_0\,\tilde{t})]}{1+\tilde{\omega}_0^2}. \tag{16}$$

Substitution of Eq. (16) into Eq. (10) with Eq. (14) and integration with respect to $\tilde{\gamma}$ from 0 to $2\pi/\tilde{\omega}_0$ yield

$$0 = \tilde{A}^2\tilde{c}\frac{\pi\tilde{\omega}_0}{1+\tilde{\omega}_0^2} + \tilde{A}^2\pi\tilde{\omega}_0\left(\tilde{a} + \frac{3}{4}\tilde{A}^2\tilde{\omega}_0^2\right). \tag{17}$$

Thus, $\tilde{A}$ is obtained as

$$\tilde{A}^2 = -\frac{4}{3\tilde{\omega}_0^2}(\tilde{a}+1). \tag{18}$$

Equations (15) and (18) are rewritten in terms of the quantities before scaling by using Eq. (12) as

$$\omega_0 = \sqrt{\frac{G_M}{I} - \frac{1}{\tau^2}}, \tag{19}$$

$$A^2 = \frac{4}{3}\frac{I\tau}{b}\frac{a\tau + I}{I - G_M\tau^2}. \tag{20}$$

Now, we analyze the experimentally obtained self-oscillation based on the above equations. Figure 11 shows the $\dot{\gamma}-\sigma$ curve measured under the same conditions as the oscillation data at 1000 Hz in Fig. 8, from which we obtained $a + \eta_M = a + \tau G_M = 3.2 \times 10^{-3}$ Pa and $b = 5.1 \times 10^{-4}\,\mathrm{Pa\,s^2}$ by the least-squares fit using Eq. (9). On the other hand, parameters ω_0 and A were obtained from Fig. 8 as $\omega_0 = 0.39\ \mathrm{s}^{-1}$ ($T = 16$ s) and $A = 0.34\,\mathrm{s}^{-1}$. From these results and Eqs. (19) and (20), we numerically obtained $G_M = 1.9 \times 10^{-2}$ Pa and $\tau = 0.98$ s, and then we numerically solved Eqs. (2) and (3) with Eq. (8) and $\sigma = 0$ using the above parameters. The result is shown in Fig. 12, in which the period T is 16 s and the amplitude A is $0.27\ \mathrm{s}^{-1}$. This result is consistent with the experimental result, $T = 16$ s and $A = 0.34\ \mathrm{s}^{-1}$.

Finally, we discuss the origin of the elasticity included in the Maxwell element. We consider disclinations, which have

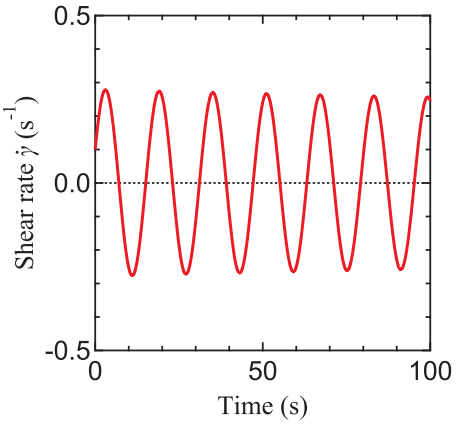

FIG. 12. Numerical result calculated using Eqs. (2) and (3). The initial condition is $\dot{\gamma} = 0.1\ \mathrm{s}^{-1}$, $\gamma = 0$, and $\sigma_M = 0$ Pa. The period of oscillation T is 16 s ($\omega_0 = 0.39\ \mathrm{s}^{-1}$) and amplitude A is $0.27\ \mathrm{s}^{-1}$.

tension that brings about the elasticity. The line tension of disclinations is given by $\sigma_{\rm line} = \pi K s^2 \log[R/r_c]$, where K is the Frank elastic constant, s is the strength of the disclination, R is the system size, and r_c is the core size of the disclination [33,34]. Substituting the typical values, $K \approx 10^{-11}$ N [35,36], $s = 1/2$, and $R/r_c \approx 10^5$, we obtain $\sigma_{\rm line} \approx 10^2$ pN. From the dimensional analysis, the elastic modulus is given by $\sigma_{\rm line}\rho$, where ρ is the line density of disclinations, that is, the length of disclinations per unit volume. At high electric fields in EBBA(H), ρ is estimated to be higher than $100\,\mu\text{m}/(100\,\mu\text{m})^3 = 10^{-4}\,\mu\text{m}^{-2}$, because we observed by microscopy at least one disclination line per $100 \times 100\,\mu\text{m}^2$ area with a gap of $100\,\mu$m. Therefore, the elastic modulus originating from disclinations is at least 10^{-2} Pa, which can explain the expected value of $G_{\rm M} = 1.9 \times 10^{-2}$ Pa. The line density may increase with the conductivity (Fig. 3), so $G_{\rm M}$ may also increase with the conductivity. This explains the experimental result that self-oscillation was observed in EBBA(H) but not in EBBA(L). Related to this, we briefly mention MBBA(P), in which the self-oscillation was not observed, although the conductivity is comparable to that of EBBA(H). In the present model, the occurrence of self-oscillation is determined by $\tilde{G}_{\rm M} = G_{\rm M}\tau^2/I$ [Eq. (12)], and $G_{\rm M}$ originates from the line tension of disclinations and τ can be regarded as the annihilation time of disclination lines. Therefore, we can ascribe the difference between EBBA(H) and MBBA(P) to different $G_{\rm M}$ and τ, which depend not only on the conductivity, but also on the Frank elastic constants and the Leslie viscosity coefficients.

V. CONCLUSION

We have investigated the conductivity dependence of negative viscosity by using ion-doped EBBA, which is a homologue of MBBA. The rheological properties were strongly dependent on conductivity. The pure sample with no dopant showed no negative viscosity, whereas the doped samples exhibited negative viscosity and rheological properties similar to those of MBBA. Microscopic observations showed that the negative viscosity appeared when the turbulence was sufficiently developed, and high conductivity was necessary for developing the turbulence. Spontaneous shear flow and N-shaped curves were observed, and the scaling relation for the N-shaped curve was confirmed in the ion-doped samples. We measured the spontaneous shear rate as a function of the amplitude and frequency of the ac electric field to create two-dimensional plots in the frequency and amplitude plane, which gave phase diagrams of the paraviscous and ferroviscous phases, indicating that the critical frequency increased remarkably with increasing conductivity. In addition, in the high-conductivity sample EBBA(H), self-oscillation occurred around the transition point. We discussed the mechanism of this self-oscillation and proposed a model with viscoelasticity, which arose from disclinations. The model reproduced the self-oscillation. However, the texture formed by the turbulence which creates the disclinations is not explicitly considered in the model. As a future work, we need to construct a mesoscopic theory of the rheological properties of textured liquid crystals in the presence of turbulence.

We identified another nematic liquid crystal, EBBA, that exhibits large negative viscosity in addition to MBBA, though an ionic dopant was necessary to increase the conductivity of EBBA. We expect that other liquid crystals with negative viscosity will be found, and that they will deepen our understanding of negative viscosity in active matter.

ACKNOWLEDGMENT

This work was supported by JSPS KAKENHI Grants No. JP25103006, No. JP26289032, No. JP15K13553, and No. JP18H01374.

[1] H. Orihara, Y. Harada, F. Kobayashi, Y. Sasaki, S. Fujii, Y. Satou, Y. Goto, and T. Nagaya, Phys. Rev. E **99**, 012701 (2019).
[2] A. Sokolov and I. S. Aranson, Phys. Rev. Lett. **103**, 148101 (2009).
[3] S. Rafaï, L. Jibuti, and P. Peyla, Phys. Rev. Lett. **104**, 098102 (2010).
[4] J. Gachelin, G. Miño, H. Berthet, A. Lindner, A. Rousselet, and E. Clément, Phys. Rev. Lett. **110**, 268103 (2013).
[5] H. M. López, J. Gachelin, C. Douarche, H. Auradou, and E. Clément, Phys. Rev. Lett. **115**, 028301 (2015).
[6] D. Saintillan, Annu. Rev. Fluid Mech. **50**, 563 (2018).
[7] J.-C. Bacri, R. Perzynski, M. I. Shliomis, and G. I. Burde, Phys. Rev. Lett. **75**, 2128 (1995).
[8] A. Zeuner, R. Richter, and I. Rehberg, Phys. Rev. E **58**, 6287 (1998).
[9] L. Lobry and E. Lemaire, J. Electrost. **47**, 61 (1999).
[10] Y. Hatwalne, S. Ramaswamy, M. Rao, and R. A. Simha, Phys. Rev. Lett. **92**, 118101 (2004).
[11] B. M. Haines, A. Sokolov, I. S. Aranson, L. Berlyand, and D. A. Karpeev, Phys. Rev. E **80**, 041922 (2009).
[12] D. Saintillan, Exp. Mech. **50**, 1275 (2010).
[13] L. Giomi, T. B. Liverpool, and M. C. Marchetti, Phys. Rev. E **81**, 051908 (2010).
[14] S. D. Ryan, B. M. Haines, L. Berlyand, F. Ziebert, and I. S. Aranson, Phys. Rev. E **83**, 050904(R) (2011).
[15] A. Loisy, J. Eggers, and T. B. Liverpool, Phys. Rev. Lett. **121**, 018001 (2018).
[16] M. I. Shliomis and K. I. Morozov, Phys. Fluids **6**, 2855 (1994).
[17] H. W. Müller and M. Liu, Phys. Rev. E **64**, 061405 (2001).
[18] E. Lemaire, L. Lobry, N. Pannacci, and F. Peters, J. Rheol. **52**, 769 (2008).
[19] H. F. Huang, M. Zahn, and E. Lemaire, J. Electrostat. **68**, 345 (2010).
[20] H. F. Huang, M. Zahn, and E. Lemaire, J. Electrostat. **69**, 442 (2011).

[21] H. Gruler, U. Dewald, and M. Eberhardt, Eur. Phys. J. B **11**, 187 (1999).
[22] S. Ramaswamy, Annu. Rev. Condens. Matter Phys. **1**, 323 (2010).
[23] M. C. Marchetti, J. F. Joanny, S. Ramaswamy, T. B. Liverpool, J. Prost, M. Rao, and R. A. Simha, Rev. Mod. Phys. **85**, 1143 (2013).
[24] H. Kneppe and F. Schneider, Mol. Cryst. Liq. Cryst. **97**, 219 (1983).
[25] V. P. Arora and V. K. Agarwal, J. Phys. Soc. Jpn. **45**, 1360 (1978).
[26] G. H. Heilmeier, L. A. Zanoni, and L. A. Barton, Proc. IEEE **56**, 1162 (1968).
[27] K. Hirakawa and S. Kai, Mol. Cryst. Liq. Cryst. **40**, 261 (1977).
[28] S. Kai and W. Zimmermann, Prog. Theor. Phys. Suppl. **99**, 458 (1989).
[29] S. Kai, W. Zimmermann, M. Andoh, and N. Chizumi, J. Phys. Soc. Jpn. **58**, 3449 (1989).
[30] S. Kai, W. Zimmermann, M. Andoh, and N. Chizumi, Phys. Rev. Lett. **64**, 1111 (1990).
[31] S. Kai, M. Andoh, and S. Yamaguchi, Phys. Rev. A **46**, R7375 (1992).
[32] T. Nagaya, T. Takeda, and H. Orihara, J. Phys. Soc. Jpn. **68**, 3848 (1999).
[33] S. Chandrasekhar, *Liquid Crystals*, 2nd ed. (Cambridge University Press, Cambridge, 1992).
[34] P. G. de Gennes and J. Prost, *The Physics of Liquid Crystals*, 2nd ed. (Oxford Science, New York, 1993).
[35] M. Greulich, G. Heppke, and F. Schneider, Z. Naturforsch., A **30**, 515 (1975).
[36] P. Sherrel and D. Crellin, J. Phys., Colloq. **40**, C3-211 (1979).